The Astrophysical Journal, 997:57 (10pp), 2026 January 20 https://doi.org/10.3847/1538-4357/ae2c85

Hemispheric Magnetic Asymmetry and Cross-equatorial Circulation Cells within the Sun's Near-surface Shear Layer

Anisha Sen[1,2], S. P. Rajaguru[1,2], Ruizhu Chen[3], Junwei Zhao[3], and Shukur Kholikov[4]
[1] Indian Institute of Astrophysics, II Block, Koramangala, Bengaluru 560 034, India; anisha.sen@iiap.res.in, rajaguru@iiap.res.in
[2] Pondicherry University, R.V.Nagar, Kalapet, Puducherry 605014, India
[3] W. W. Hansen Experimental Physics Laboratory, Stanford University, Stanford, CA 94305-4085, USA
[4] National Solar Observatory, Boulder, CO, USA
Received 2025 October 3; revised 2025 November 21; accepted 2025 December 12; published 2026 January 14

Abstract

Using time–distance helioseismic measurements of meridional flow in the near-surface shear layer over a period of 14 yr starting from 2010 May, we probe the depth structure and evolution of its cross-equatorial part. We confirm that the hemispheric magnetic asymmetry determines the amplitude and direction of such flows. Additionally, we find that these flows turn over and change direction at depths below $0.97R_{\odot}$ forming circulation cells with lifetimes dictated again by the hemispheric magnetic imbalance, which is dominated by the occurrences of large sunspots. We also examine connections between cross-equatorial magnetic flux plumes and flows and discuss their implications for the equatorial flux cancellation/submergence and the poleward transport of flux.

Unified Astronomy Thesaurus concepts: The Sun (1693); Helioseismology (709); Sunspots (1653); Solar meridional circulation (1874); Solar interior (1500); Solar physics (1476); Solar convective zone (1998)

1. Introduction

Global scale meridional flow (T. L. Duvall 1979; D. H. Hathaway & L. Rightmire 2010; J. Zhao et al. 2013; S. Kholikov et al. 2014; S. P. Rajaguru & H. M. Antia 2015; R. Chen & J. Zhao 2017) is well recognized as a key player in the magnetic flux transport processes (see, e.g., Y. M. Wang et al. 1989; M. Dikpati & P. A. Gilman 2006; A. R. Yeates et al. 2023) on the Sun. In the near-surface layers, it carries flux from decaying active regions, typically the trailing-polarity fields of tilted bipolar regions, toward the poles, where they cancel oppositely oriented fields of the previous solar cycle and drive the reversal of the Sun's polar magnetic fields (Y. M. Wang et al. 1989; D. H. Mackay & A. R. Yeates 2012). While we still lack a complete understanding of the origin and maintenance of meridional circulation on the Sun, on average, it is modeled as a hemisphere-antisymmetric flow system with a vanishing meridional component at the equator. However, in reality, on timescales of the lifetimes of active region complexes, which have hemispheric asymmetry, prominent cross-equatorial flows are observed (R. Komm 2022). Such flows are thought to play a significant role in transporting opposite-polarity magnetic flux across the equator, facilitating magnetic flux cancellation (A. A. Norton et al. 2014). Some studies indicate that the total flux canceled at the equator directly correlates with the net flux transported to the poles (R. H. Cameron & M. Schüssler 2012; S. K. Bisoi & P. Janardhan 2020). Earlier studies had linked substantial deviations in the average meridional flow at the equator to minor systematic errors in telescope alignment at single-site, ground-based observations (R. W. Komm et al. 1993). However, modern helioseismic instruments have undergone rigorous alignment verification, including validation through planetary transits for Global Oscillation Network Group (GONG; C. G. Toner 2001; C. Toner et al. 2004) and the Helioseismic and Magnetic Imager (HMI) onboard the Solar Dynamics Observatory (SDO; S. Couvidat et al. 2016; J. T. Hoeksema et al. 2018). Such precise calibrations ensure reliable measurement of small meridional flow variations near the equator. Through ring diagram analysis of Dopplergrams from the Michelson Doppler Imager (MDI) Dynamics Program, the GONG and HMI, R. Komm (2022) reported significant cross-equatorial meridional flows toward the hemisphere with larger magnetic flux, to depths down to 10 Mm. Using solar-cycle-long time–distance (TD) helioseismic measurements of meridional flows in the Sun's near-surface shear layer (NSSL), A. Sen et al. (2025) identified that near-surface inflows toward active latitudes are part of a localized circulation, which has an outflow away from active latitudes at depths of approximately $0.97R_{\odot}$ (20 Mm). These authors also showed that such active region flows, under the action of Coriolis force, explain the depth profile of deviations in the radial gradient of rotation measured in global helioseismic studies (H. M. Antia & S. Basu 2022).

Investigating the dynamics of active region driven circulation cells near or across the equator (D. A. Haber et al. 2004; B. W. Hindman et al. 2009; D. C. Braun 2019) and their variations in response to hemispheric asymmetry of magnetic flux is essential to understanding the flux cancellation process and the resulting global evolution of solar cycle magnetic field (R. H. Cameron & M. Schüssler 2012). In this paper, we examine the depth profiles of cross-equatorial flows within the NSSL using TD helioseismic measurements and investigate the extent to which these flows are influenced by large-scale inflows toward active regions, offering insights into their role in solar dynamics and internal flow variations. The rest of the paper is structured as follows: Section 2 outlines the data utilized and a description of the analysis technique. Section 3 presents our findings, and Section 4 discusses the implications of our results.

2. Data and Analysis Procedure

The data and analysis procedure are the same as those used and explained by A. Sen et al. (2025). Briefly, using identically processed helioseismic data from the space-borne HMI (P. H. Scherrer et al. 2012) aboard NASA's SDO and from

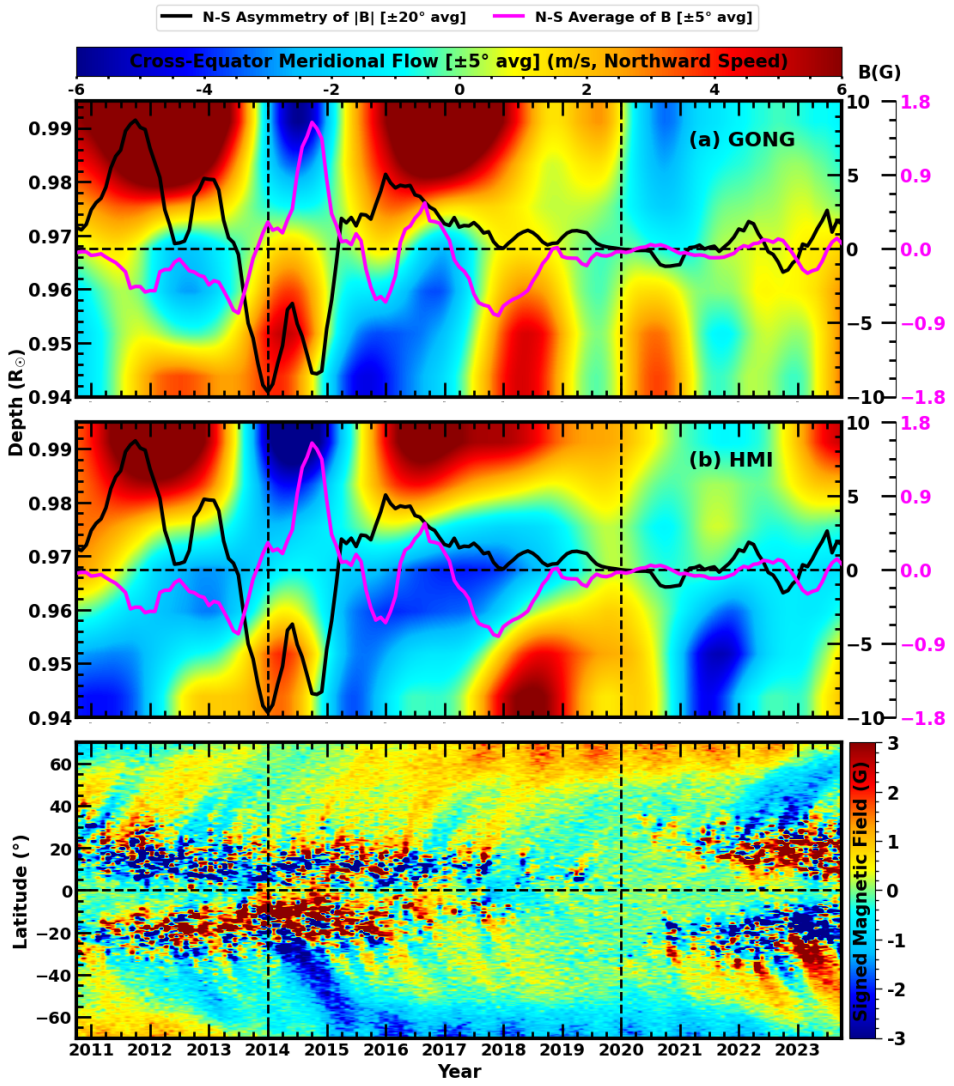

Figure 1. Time–depth profiles of meridional flow, U_θ, averaged over ±5° across the equator, are shown in the top two panels that compare measurements from GONG and HMI. Positive (negative) values represent northward (southward) flows, and the depth range covers the whole of the near-surface shear layer. The bottom panel shows the magnetic butterfly diagram derived from the HMI LOS magnetic field, denoted simply as B, for the same period. The overplotted black and pink curves, with right y-axes, are the time variations' N–S asymmetry in the absolute hemispheric magnetic field averaged over active latitudes (±20°), $<|B|_N> - <|B|_S>$, and the N–S average of signed magnetic field over the equator (±5°), respectively. Both curves have been smoothed using a 6 month running average.

the ground-based GONG, we perform TD helioseismology (T. L. Duvall et al. 1993) to measure meridional flows (S. P. Rajaguru & H. M. Antia 2015) within the NSSL. The data covers a 14 yr period from 2010 May to 2024 April. Our measurements are at a binned-down spatial resolution of $0.^\circ 36$ pixel^{-1} for both HMI and GONG. To take care of the surface magnetic effect in flow measurements (Z.-C. Liang & D.-Y. Chou 2015; R. Chen & J. Zhao 2017), we mask out active regions in input Doppler data that exceed a threshold of 40 G in the 0.36 deg pix^{-1} resolution HMI LOS magnetograms. We further note that we recover meridional flows from the inversions for the stream function, which satisfies the continuity equation and thus the mass conservation constraint is built into the inversion scheme (S. P. Rajaguru & H. M. Antia 2015).

We also utilize local TD helioseismic inversions for horizontal velocity fields (J. Zhao et al. 2012b), available through the JSOC TD helioseismology pipeline.[5] Additionally, we analyze HMI line-of-sight magnetograms to investigate the temporal and latitudinal variations of magnetic flux. To compare time–latitude profiles of cross-equatorial flows with sunspot distributions, we use data from the National Oceanic and Atmospheric Administration (NOAA) Solar Region Summary.

3. Results

3.1. Cross-equatorial Flows: Structure, Evolution, and Active Region Connections

A primary objective in this work is to probe the depth structure of cross-equatorial meridional flows. Time–depth profiles of equator-crossing part of meridional flow, U_θ, averaged over ±5° across the equator and covering the whole depth range of the NSSL, are shown in the top and middle panels of Figure 1 for the GONG and HMI measurements, respectively. The sign convention of positive values for northward flow in both hemispheres is used, and a 12 month

[5] http://jsoc.stanford.edu/data/timed/

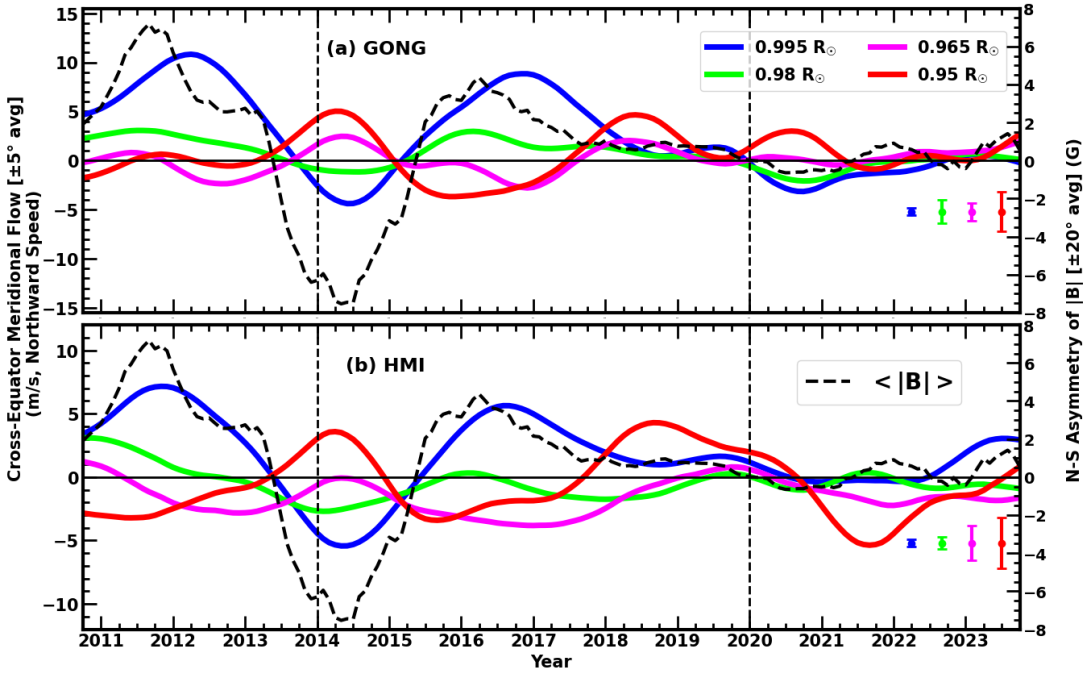

Figure 2. Cuts across different depths of the 2D time–depth profile of cross-equatorial flows shown in Figure 1 for GONG and HMI: blue (0.995 $R_\odot$), green (0.98 $R_\odot$), magenta (0.965 $R_\odot$), and red (0.95 $R_\odot$). The estimated error for each depth is marked within the panels. The dashed black curve in both panels is the same as in Figure 1, except that here we have applied a 12 month running average, and it corresponds to the right *Y*-axis.

running average has been applied for the flow measurements. A very good agreement of flow measurements from the two independent data sources is clear.

To study the connections to magnetic flux, we generate the magnetic butterfly diagram using the HMI LOS magnetic fields, denoted simply as B, and it is shown in the bottom panel of Figure 1. The hemispheric asymmetry in the magnetic field is estimated by taking the difference between the absolute magnetic field averaged over active latitudes (0°–20°) in the north and south, $B_{\rm asym} = <|B|_N> - <|B|_S>$. We also calculate the *N*–*S* average of the signed magnetic field over the equator (±5°), $B_{\rm eq}$, which represents the cross-equatorial flux plumes (R. H. Cameron et al. 2013; S. K. Bisoi & P. Janardhan 2020), to examine their connections to the cross-equatorial flows. Both these quantities are overplotted as black and pink curves in Figure 1, with values in the right *Y*-axes. We discuss the connections between cross-equatorial flows and flux plumes ($B_{\rm eq}$) in Section 3.2.

Positive hemispheric asymmetry ($B_{\rm asym} > 0$), in our convention, corresponds to the northern hemisphere being more active than the southern hemisphere and vice versa. The horizontal dashed line is the zero level for hemispheric asymmetry (right *Y*-axis). First, we confirm the earlier result (R. Komm 2022) that the cross-equatorial flow changes in response to the hemispheric asymmetry in magnetic flux: a higher level of northern hemispheric flux during the rising phase of Cycle 24 (2011–2013) caused north-directed near-surface flow across the equator, an opposite situation during the maximum phase (2013–2015) and again back to north-directed near-surface flow in the declining phase (2016–2018). The agreement between GONG and HMI measurements is striking, both in terms of magnitudes and lifetimes of flow structures: a period of about 2 yr and a magnitude of about 8 m^{-1}. Most interestingly, we find that these flow structures correspond to cross-equatorial circulation cells with return flows roughly at depths below 0.97 $R_\odot$. To better illustrate the flow amplitudes and their changes over depth, we plot in Figure 2 cuts across different depths of the 2D time–depth profile of cross-equatorial flows shown in Figure 1: blue (0.995 $R_\odot$), green (0.98 $R_\odot$), magenta (0.965 $R_\odot$), and red (0.95 $R_\odot$). The error bars shown in Figure 2 are derived from an analysis of inverted flow velocities obtained by repeating the inversion 1000 times, with travel times randomly perturbed using the estimated uncertainties in the observed values (S. P. Rajaguru & H. M. Antia 2015). This estimated error for each depth is marked within the panels. The dashed black curve in both panels is the same as in Figure 1 and corresponds to the right *Y*-axis. In contrast to Figure 1, a 12 month running average has been applied to the dashed black curve (right *y*-axis) to compare with the flow cut (left *y*-axis), which is averaged over the same period. It is clear that the flow profile at the upper layer is strongly positively correlated with the hemispheric magnetic asymmetry, whereas at the deeper layer within the NSSL, it is anticorrelated, with the change-over happening near 0.965–0.97 $R_\odot$. Between 0.97 $R_\odot$ and 0.94 $R_\odot$, the flow profile keeps its direction, remaining negatively correlated with the hemispheric absolute magnetic asymmetry.

3.2. Connections between Cross-equatorial Flows and Flux Plumes

During active phases, especially during the maximum phase of a solar cycle, there are cross-equatorial exchanges of magnetic flux, which have been analyzed by R. H. Cameron et al. (2013) and S. K. Bisoi & P. Janardhan (2020). But neither study had knowledge of cross-equatorial meridional flows as a fairly long-lived phenomenon, whose existence

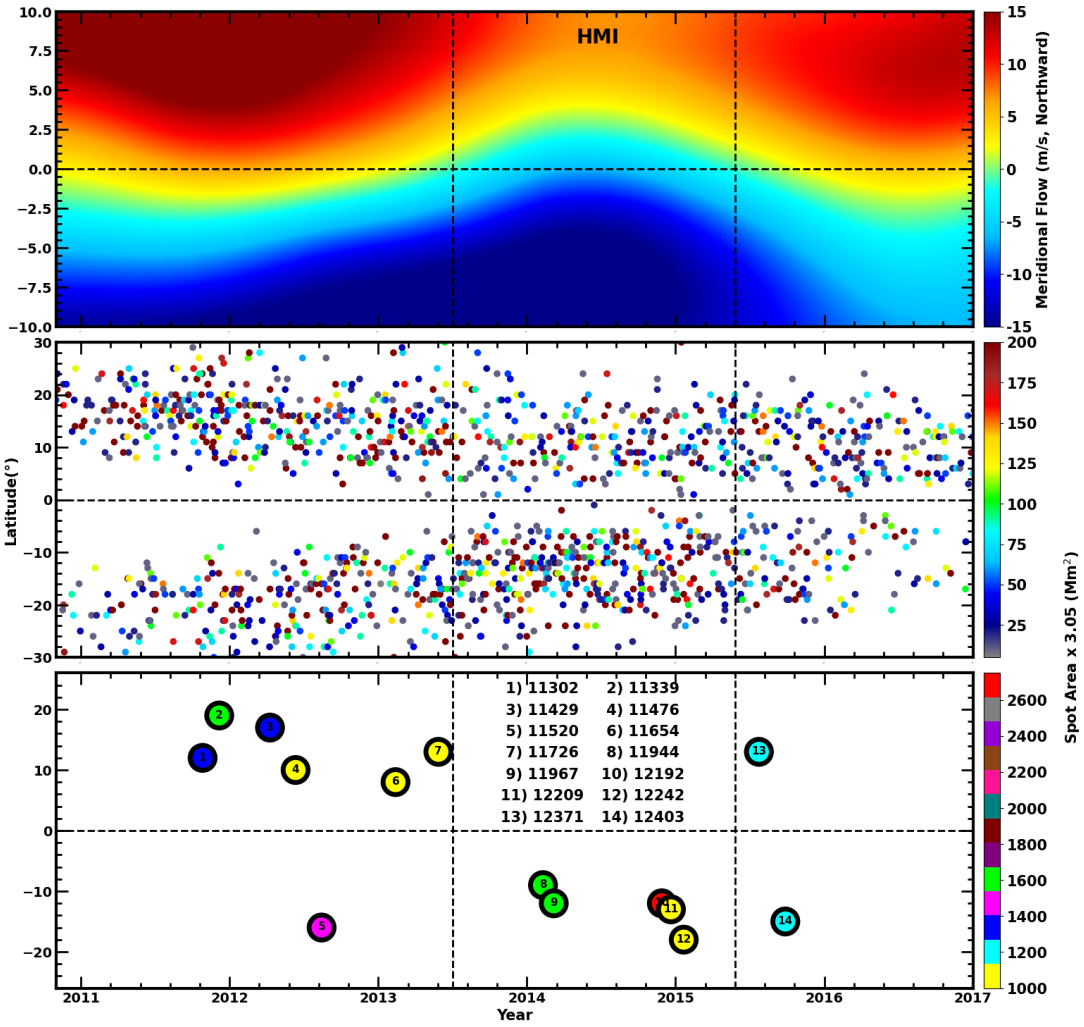

Figure 3. Time–latitude profile of near-surface (0.99 $R_\odot$) meridional flow (over $\pm 10^\circ$ across the equator) is compared with that of sunspot locations and sizes. The time period chosen (2011–2017) is that of the active phase of Solar Cycle 24. The middle panel displays the locations and sizes of all sunspots, with the colorbar restricted to 200 millionths of a hemisphere (μHS), while the lower panel shows that of large sunspots with an area greater than 1000 millionths of a solar hemisphere. The NOAA sunspot group numbers of the large spots are listed within the panel. The two vertical dashed lines mark the time of change in flow direction across the equator.

was reported in later studies. Moreover, our findings here that these flows are part of circulation cells warrant a closer look at the connections between flux plumes and flows. However, R. H. Cameron et al. (2013) did address the combined roles of flux emergence, advection, and diffusion in the transport of magnetic flux across the equator, and, in particular, demonstrated that cross-equatorial flux plumes constitute sudden injections of flux that cannot be explained as a diffusion process. As shown in Figure 3, the largest sunspot groups (bottom panel) that drive cross-equatorial flows typically emerge away from the equator, while only a few smaller groups appear close to the equator (middle panel), some of which deviate from Joy's law. During cycle 24, however, we find that most flux plumes followed the leading polarity of the source hemisphere. This indicates that, in this case, the cross-equatorial flux plumes are not attributable to emergence or diffusion processes; instead, advection appears to be the dominant mechanism responsible for their occurrence. To address this further, in this section, we probe the connections between the cross-equatorial flows and flux plumes.

The time variation of cross-equatorial flux plumes, $B_{\rm eq}$, is captured by the overplotted pink curve in Figure 1. For solar cycle 24, the leading polarity of the southern hemisphere was positive (red; see bottom panel of Figure 1). During the maximum of this cycle (2013–2015), the southern hemisphere was more active ($B_{\rm asym} < 0$) while the cross-equatorial flux plumes are dominantly positive, i.e., the leading polarity flux of the southern hemisphere is transported northward across the equator. During 2011–2013, when the northern hemisphere was more active ($B_{\rm asym} > 0$), the flux plumes were negative, corresponding to leading polarity flux from the northern hemisphere crossing the equator. A similar episode of negative flux plumes across the equator happened during 2016–2017 (when $B_{\rm asym} > 0$). These observations, thus, show that the cross-equatorial surface flows and magnetic flux plumes are in opposite directions. However, our findings that cross-equatorial flows are part of circulation cells, which have returning flows at depths below 0.97 $R_\odot$, indicate that the flux plumes

actually are dragged by these outflows at the deeper layers of the NSSL, where the active region magnetic flux is rooted. In summary, hemispheric magnetic asymmetry enhances inflows toward the more active hemisphere in the upper layer, while outflows in the deeper layer drag the magnetic flux plumes along with them, in the direction opposite to the surface inflows.

3.3. Sunspots and Cross-equatorial Flows

In this section, we attempt a detailed analysis of how the locations and areas of sunspots are linked to cross-equatorial flows. We explore the extent to which the distribution and size of sunspots influence the strength and direction of these flows, shedding light on the underlying mechanisms that govern their interaction. The top panel of Figure 3 shows the zoomed-in view of the cross-equatorial flow during the cycle maxima (2010 October–2016 December) at a depth of $0.995R_{\odot}$. Two vertical dashed black lines indicate the flow direction change across the equator. From 2010 October to 2013 May, the flow was directed toward the northern hemisphere. Between 2013 June and 2015 May, it shifted toward the southern hemisphere. From 2015 June to 2023 October, the flow remained directed northward. In the middle panel of Figure 3, we present the locations of sunspots over the same period mentioned above. The spot area is indicated on the colorbar, with a restricted upper limit of 200 millionths of the hemisphere, equivalent to 200×3.05 (Mm^2).

When the flow is directed toward the northern hemisphere, sunspots in the southern hemisphere become more widely dispersed over time, as the flow carries away a significant portion of the magnetic flux. In contrast, sunspots in the northern hemisphere tend to remain more clustered. A similar pattern is observed during southward-directed flow, with the roles reversed. R. Komm (2022) reported that during Solar Cycle 23, the cross-equatorial was predominantly directed toward the southern hemisphere, whereas in Solar Cycle 24, it was mostly directed northward. Our analysis aligns with previous findings, confirming that during Solar Cycle 24, the southward flow persisted for approximately 2 yr (from 2013 June to 2015 May). However, for the majority of the observed period, the flow was directed northward. We also identified a contributing factor: throughout the cycle, the distance between the activity belt in the northern hemisphere and the equator remained significantly smaller than in the southern hemisphere. Between 2010 October and 2016 December, a total of 1492 NOAA sunspot groups were recorded. From these, we selected the top 1% of the largest groups, specifically those with an area exceeding 1000 millionths of the hemisphere. Based on this criterion, we identified 14 sunspot groups.

In the lower panel of Figure 3, we have plotted the largest sunspot groups, with their areas indicated in the colorbar and group numbers labeled within the figure. Notably, sunspots with areas exceeding 1000 millionths of the hemisphere appear in the photosphere approximately 8 to 12 months after the onset of cross-equatorial flow in the upper layers. For instance, during the northward flow that began in 2010 October, the first large sunspot group emerged in 2011 September (AR: 11302, Date: 2011 September 25, Latitude: 12°N, Area: 1300 μHS). When the cross-equatorial flow was directed southward, the first major sunspot group appeared in 2014 January (AR: 11944, date: 2014 January 9, latitude: 9°S, area: 1560 μHS), following the onset of the southward flow in 2013 June. We also found that sunspots with areas exceeding 1000 millionths of the hemisphere predominantly form within a latitude range of 8°–25° in both hemispheres. The presence of larger sunspots near the equator was likely the primary driver of the cross-equatorial flow. A greater number of large sunspots was observed in the northern hemisphere when the flow was directed northward, while more large sunspots appeared in the southern hemisphere when the flow was directed southward.

3.4. Tests Removing Active Region Contributions to Cross-equatorial Flows

Questions on the level of contributions from flows around active regions to variations in large-scale meridional flows are still not answered satisfactorily, as there are contradicting results from different analyses (B. W. Hindman et al. 2009; D. C. Braun 2019; P. L. Poulier et al. 2022; S. S. Mahajan et al. 2023). Here, we attempt an investigation into the extent of active region contributions to cross-equatorial flows by employing the 3D (latitude, longitude, and depth) local TD helioseismic inversions for horizontal velocity fields available in the JSOC TD helioseismology pipeline (J. Zhao et al. 2012b), which facilitates deriving longitudinally averaged cross-equatorial flows after removing active regions and their surroundings. The chosen time period is 2010 October–2016 December. First, we remove the center-to-limb systematics (J. Zhao et al. 2012a; R. Chen & J. Zhao 2018) in these full-disk flow maps, stacked from $30^{\circ} \times 30^{\circ}$ tiles, and the large-scale time-averaged background rotation signal following S. S. Mahajan et al. (2023).

We then derive longitudinally averaged meridional flows for each Carrington rotation before and after removing the active regions and their surroundings, as illustrated in Figure 4. We excluded a total of 1492 NOAA sunspot groups observed between 2010 October and 2016 December, covering their entire lifetimes. For each group, all occurrences were removed within $40^{\circ} \times 40^{\circ}$ windows, centered on the corresponding active region flux centroid retrieved from the Space-Weather HMI Active Region Patches (M. G. Bobra et al. 2014) database. During the cycle maximum period, however, such active region removal leads to situations of running out of data points or with very few points being averaged (see also S. S. Mahajan et al. 2023) resulting in artificially enhanced flow values relative to the case of full average. To remedy this situation, we estimate a baseline quiet-Sun meridional flow profile, over latitude and depth, by averaging over a 1 yr period during Cycle 24 minimum (mid-2019 to mid-2020; there still were a few small active regions, and we masked them out) and assign it to all identified active region locations that are set for removal. This procedure ensures consistency in the pixel statistics before and after the removal of active regions, as the total number of pixels averaged remains the same. The estimated baseline profile is shown in Figure 5, which compares well with that determined by S. S. Mahajan et al. (2023).

We show the results of the above exercise in Figure 6: the temporal variation of the cross-equatorial flow at the near-surface depth of 3.5 Mm (average over the first three depths at 1, 0.995, and 0.99 $R_{\odot}$) in the top left panel and the depth profile of the same near the equator in the top right panel.

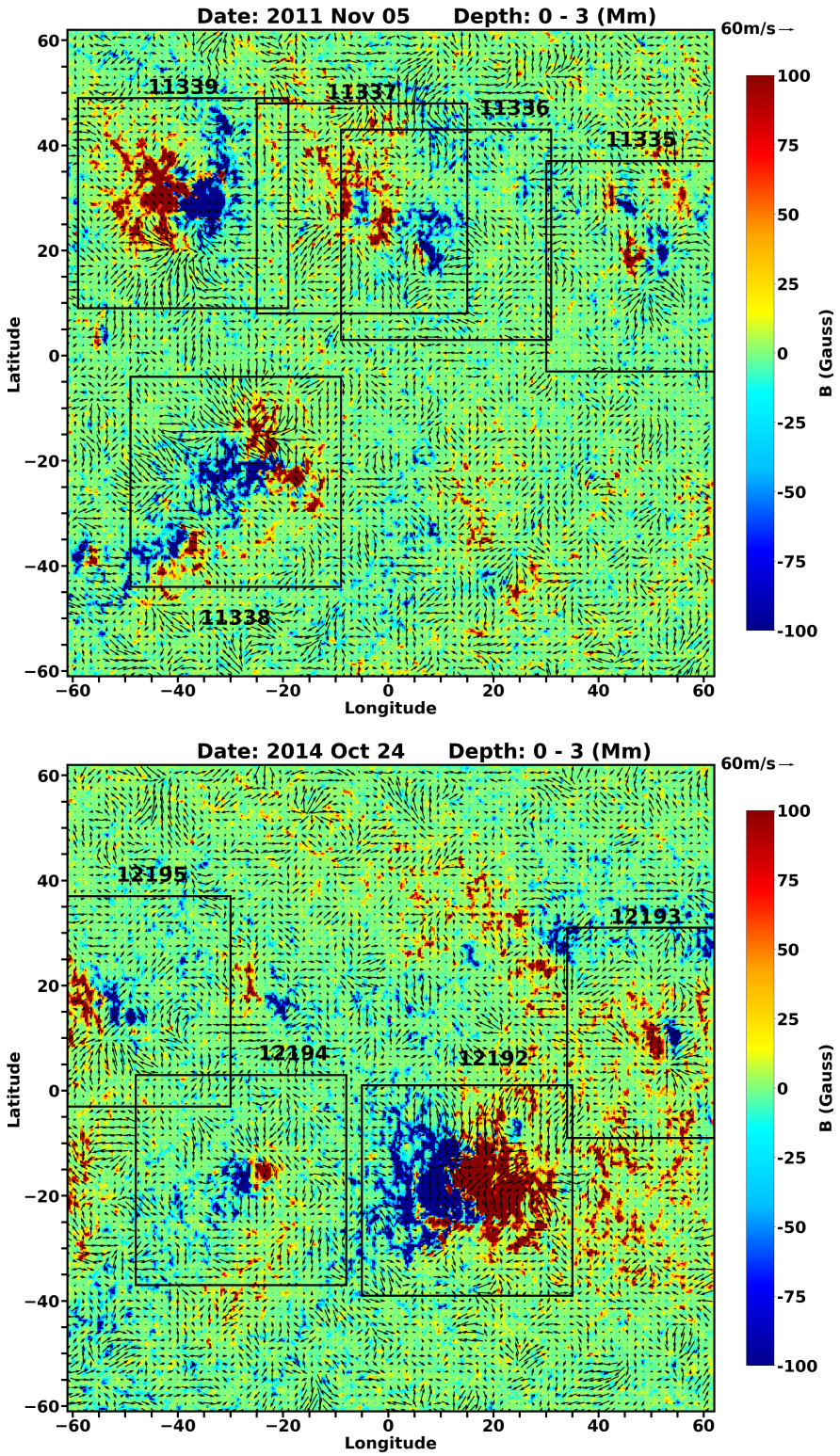

Figure 4. Examples depicting how sunspot regions and their surroundings are removed in flow maps before longitudinally averaging them to test the extent of contributions from flows around active regions to the cross-equatorial flows. This test is performed on the local 3D (latitude, longitude, and depth) time–distance helioseismic flow inversions that map the upper 20 Mm of the convection zone. The two panels correspond to dates when episodes of large cross-equatorial flows were measured.

Here, a 12 month running average has been applied to compare with Figure 1; the lower panels show flows recovered after the active regions and their surroundings have been removed and replaced by baseline (quiet-Sun) flows as explained above. Comparing the upper and lower panels, we find that, although the cross-equatorial flow signal has decreased significantly after removing the active regions, a residual flow pattern remains. Similarly, the two black curves (solid and dashed) in

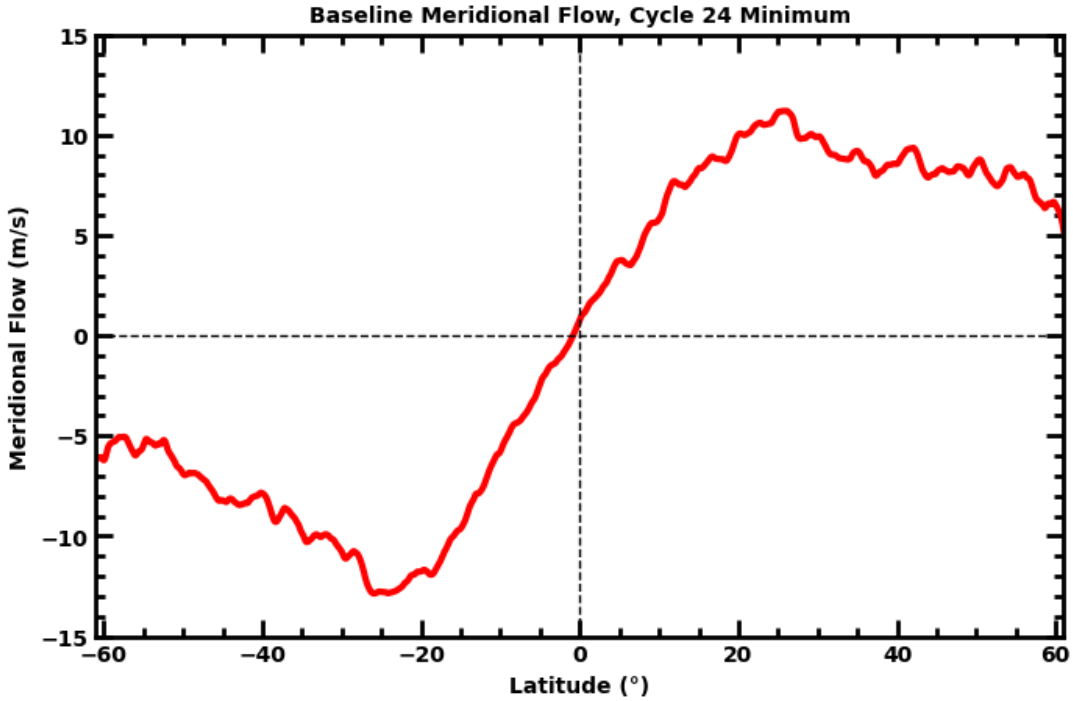

Figure 5. Baseline quiet-Sun meridional flow profile at a depth of 3.5 Mm determined by averaging over a 1 yr period during Cycle 24 minimum (mid-2019 to mid-2020).

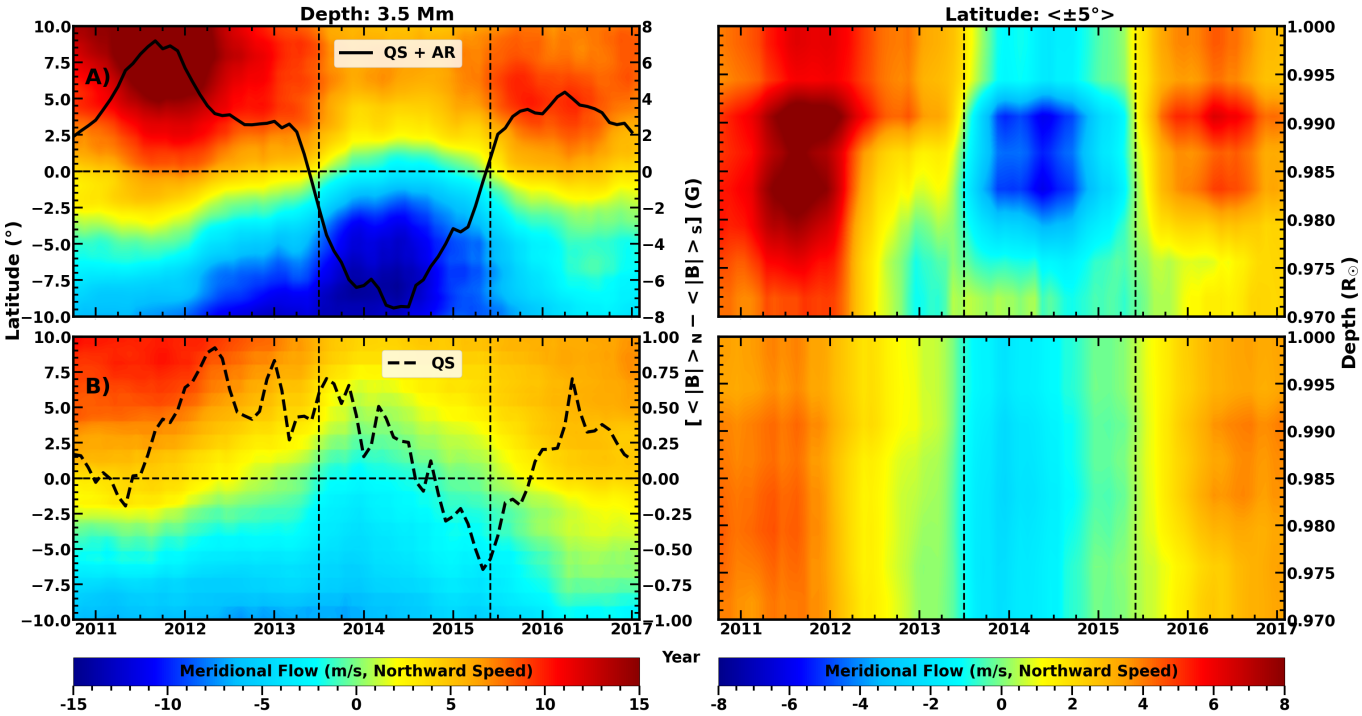

Figure 6. Comparison of cross-equatorial flow structures before (upper panels) and after removing active regions and their surroundings (40° × 40° area; lower panels). These results are from the local 3D (latitude, longitude, and depth) time–distance helioseismic flow inversions that map the upper 20 Mm of the convection zone, and the chosen time period (2011–2017) covers the active phase of Solar Cycle 24. Time–latitude profiles of the meridional flow at a near-surface depth (of 3.5 Mm, corresponding to the average over the first three depth points at 1, 0.995, and 0.99 $R_\odot$) are in the left column, and the time–depth profiles covering 0.97 to 1 $R_\odot$ are in the right one. The two black curves (solid and dashed) represent the asymmetry in absolute magnetic fields with and without active regions, and the two vertical dashed black lines are the same as in Figure 3.

Figure 6, which represent the asymmetry in absolute magnetic fields with and without active regions, reveal that the asymmetry pattern also persists after removing the active regions, albeit with a slight temporal offset. This perhaps suggests that when sunspots decay into network and internetwork fields (A. Sen & S. P. Rajaguru 2023), the residual

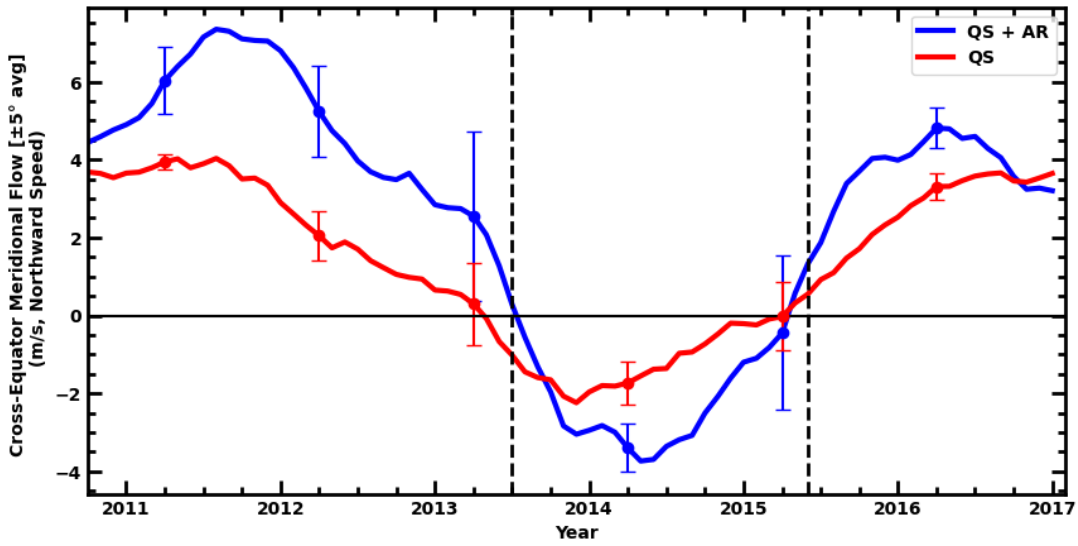

Figure 7. Comparison of cross-equatorial meridional flow profiles (at a depth of 3.5 Mm) before (blue, i.e., the whole Sun) and after removing (red) the active regions (see the text for details). Error bars here correspond to the standard errors determined from the standard deviation of individual flow measurements over 1 yr bins.

magnetic flux continues to maintain a north–south asymmetry, contributing to the cross-equatorial flow. Removal of active regions reduced the asymmetry by about ±7 G, with a residual asymmetry roughly at the ±1 G level. To make a further quantitative comparison of flow profiles before and after the removal of active regions, we plot in Figure 7 the near-surface (average of first three depths covering 0–7 Mm) cross-equatorial flow averaged between 5°S and 5°N depths. The profiles prior to and after active region removal are shown in blue and red, respectively, with error bars representing the standard deviation of measurements within a 1 yr bin. Depths up to 7 Mm were considered because the strongest inflows occur within the 3.5–7 Mm range (see Figure 8). The comparison indicates that although the flow amplitude decreases markedly after the removal of active regions, it does not vanish entirely. We discuss this further and other possible causes in Section 4.

To further test the contributions of active regions, we examine flow structures averaged over individual CRs (or months). Among the 14 largest sunspot groups plotted in the bottom panel of Figure 3, we selected the NOAA sunspot group AR 12192 (date: 2014 October 27, latitude: 12°S, area: 2750 μHS), as it was the largest spot during cycle 24. Using local TD flow maps again, we examine the flow structure across the different depths throughout the full month of its occurrence. Figure 8 presents a detailed analysis of the cross-equatorial flow during 2014 October. The top panels of Figure 8 show the one-month averaged latitude-depth flow profile before removing the active region, while the bottom panels present the profile after removing the largest spot, AR 12192. The x-axis represents depth (0–21 Mm), while the y-axis indicates latitude. The left panels cover the range from 30°S to 30°N, and the right panels provide a zoomed-in view spanning 10°S to 10°N. In the left panels, the latitude of the largest sunspot group is marked with a horizontal dotted black line. The right y-axis of the right panels shows the meridional flow velocity at the equator (latitude 0°), depicted by the magenta curve. During 2014 October, the cross-equatorial flow was negative, indicating a flow directed toward the southern hemisphere. Figure 8 reveals that the cross-equatorial flow primarily originates from deeper layers in the opposite hemisphere, extending over a broad latitudinal range compared to the surface flow. In 2014 October, when the flow was directed southward, a southward (−ve) flow was observed in the deeper layers of the northern hemisphere, extending up to latitudes of 0°–10°N. We also observed inflows toward active region 12192, as indicated by the black dotted horizontal lines at 12°S. Notably, inflows originating from higher latitudes and moving toward active regions exhibit maximum amplitude within the 5–7.5 Mm depth range, while their amplitude significantly decreases in the shallower 0–5 Mm layer. This suggests that a substantial portion of these inflows originates from deeper layers within the 5–7.5 Mm range. Additionally, equatorial inflows, those approaching active regions from the equatorial side, display greater amplitude than inflows from higher latitudes. In contrast, outflows become prominent at depths of approximately 12 Mm and extend into deeper layers, with stronger amplitudes at higher latitudes. Meanwhile, outflows directed toward the equator exhibit lower amplitude compared to those occurring at higher latitudes. The strength of the equatorial outflow also depends on the area of the sunspot group.

The bottom panels of Figure 8 show the same flow profiles as the top panels, but after removing the largest sunspot group, AR 12192. A direct comparison reveals substantial changes in the flow patterns linked to this active region. In particular, the magnitude of inflows toward the active region decreases notably after its removal. The strong equatorial outflow associated with AR 12192, clearly visible in the top panels, disappears entirely in the bottom panels, highlighting a major alteration in the large-scale flow structure. To quantify this change, we examine the cross-equatorial flow shown by the magenta curves in the right panels, with the solid line representing the flow before removal and the dashed line after. These curves, plotted on the right y-axis, demonstrate a

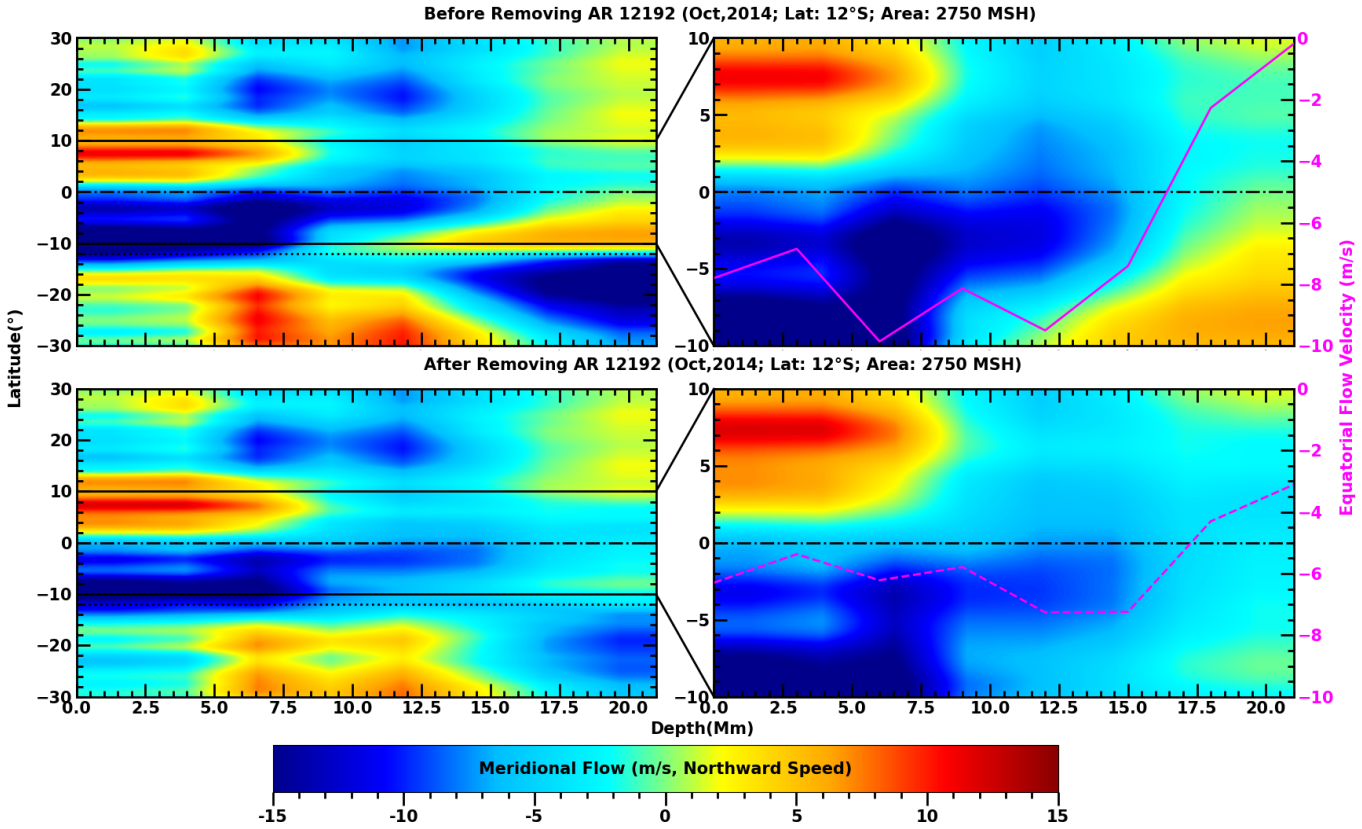

Figure 8. One-month averaged flow maps over 0–21 Mm depth, shown before (top panels) and after (bottom panels) removing the largest active region (AR 12192). In the left panels, the dotted line marks the latitude of the active region and the dashed line marks the equator. The right panels show the corresponding zoomed-in region (10°S–10°N), with equatorial flow velocities overplotted in magenta on the right *y*-axis.

reduction of about 3 m s^{-1} following the exclusion of AR 12192.

4. Discussion and Conclusion

Using TD helioseismic measurements of global-scale meridional flows (A. Sen et al. 2025), we have examined the cross-equatorial part of these flows to depths down to $0.94R_{\odot}$, covering the whole NSSL over a period of 14 yr starting from 2010 May. Measuring such flows should be free of leakage of solar rotation caused by error in the position angle (P-angle) due to instrumental misalignment. For example, a southward flow signal of about 5 m s^{-1} across the equator was detected in early TD helioseismic studies using data from the MDI onboard SOHO and was identified as due to a small misalignment of about $0.^{\circ}2$ in the orientation of the MDI instrument (P. M. Giles et al. 1997; P. M. Giles 2000; D. H. Hathaway & L. Rightmire 2010; Z.-C. Liang et al. 2017). As indicated in Section 1, both the HMI and GONG datasets used here have undergone rigorous alignment verifications employing planetary transits, ensuring reliable measurement of meridional flow variations near the equator. Combining MDI, GONG, and HMI data, R. Komm (2022) performed ring diagram analyses of meridional flows covering Cycles 23 and 24 and the early part of Cycle 25 and established that meridional flows have cross-equatorial excursions, which, at depths shallower than 10 Mm, are directed toward the hemisphere with stronger magnetic flux. The same author also identified them as driven by inflows toward active regions. Here, we have confirmed and extended earlier findings. During Cycle 24, enhanced magnetic activity in the southern hemisphere systematically drove near-surface flows across the equator in the southward direction, with amplitudes of about 8 m s^{-1} and a lifetime of about 2 yr. A striking agreement is observed between GONG and HMI results. Importantly, our measurements have imaged the whole of NSSL, revealing a flow reversal around 0.97 $R_{\odot}$. Flows in the upper NSSL are positively correlated with magnetic asymmetry, while anticorrelated with it beneath 0.97 $R_{\odot}$, forming cross-equatorial circulation cells with return flows at deeper layers. These results highlight a dynamic coupling between surface magnetic asymmetry and meridional flow structures throughout the NSSL, with indications that the deeper outflows away from active latitudes play dominant roles in the driving of circulation as well as in the transport of magnetic flux at the surface layers (see below).

Magnetic flux transport generally occurs through a combination of emergence, advection, and diffusion. R. H. Cameron et al. (2013) had, in fact, examined these processes and concluded that cross-equatorial flux plumes largely represent sudden, nondiffusive injections of flux. In our observations here, during the maximum phase of solar cycle 24, most flux plumes were carried from the more active southern hemisphere toward the northern one. Notably, these plumes were transported in the direction opposite to the near-surface cross-equatorial flows. This apparent contradiction can be reconciled by considering circulation cells: near-surface inflows converge toward the more active hemisphere, while at deeper layers (below 0.97 $R_{\odot}$), return flows or outflows drag the flux plumes across the equator in the opposite direction. We also note that

the deep-rooted magnetic flux is more passively advected at depths where high plasma β conditions prevail, and hence the deep-layer advection emerges as the dominant mechanism governing the transport of cross-equatorial flux plumes that are observed at the surface.

The contribution of active regions to large-scale meridional flow variations remains debated, with earlier studies offering conflicting results. Using 3D TD helioseismic inversions from the JSOC pipeline (2010–2016), we investigated cross-equatorial flows before and after removing active regions and their surroundings. Although the amplitude of the flow decreases after removal, the overall flow pattern and magnetic asymmetry remain. Removal of active regions reduces the asymmetry by ± 7 G, but a residual asymmetry of ± 1 G persists, suggesting that decayed sunspots to network and internetwork fields maintain the asymmetry. During cycle maximum, it becomes particularly challenging to eliminate all magnetic regions, especially those associated with preemergence and postemergence phases. N. Gottschling et al. (2021) reported that near-surface converging flows of approximately 20–30 m s^{-1} become detectable about one day prior to flux emergence. Similarly, we may expect active region flows to persist for a while after the sunspot flux bundle submerges or disperses. In our analysis, the removal of active regions has not covered the above preemergence and postdecay or submergence periods of active regions. The omission of these phases may explain the persisting cross-equatorial flows after the removal of active regions. A more detailed investigation of the preemergence and decay phases is essential to better constrain and reduce this effect.

We may also speculate on the possibility of magnetic fields confined within the NSSL but have not fully emerged to the photosphere. Such hidden flux, though not directly visible at the surface, can still play a significant role and contribute to the observed effects. Our tests removing active region areas further imply that the primary driver of cross-equatorial flows may lie in deeper layers; outflows associated with magnetic flux accumulation at the base of the NSSL could be the real source. Importantly, such deeper outflows may exist even in the absence of corresponding emerged flux-forming sunspots above them, meaning their contribution cannot be eliminated simply by masking active regions at the surface. These deeper outflows can still drive circulation cells whose surface manifestations produce cross-equatorial flows, thereby maintaining the observed pattern.

Acknowledgments

The HMI data used are courtesy of NASA/SDO and the HMI science teams. Data preparation and processing have utilized the Data Record Management System (DRMS) software at the Joint Science Operations Center (JSOC) for NASA/SDO at Stanford University. Our sincere thanks go to H.M. Antia for supporting A.S. in performing the inversions. The GONG data used are obtained by the NSO Integrated Synoptic Program, managed by the National Solar Observatory, which is operated by the Association of Universities for Research in Astronomy (AURA), Inc., under a cooperative agreement with the National Science Foundation and with contributions from the National Oceanic and Atmospheric Administration. This work has received funding from the NASA DRIVE Science Center COFFIES Phase II CAN 80NSSC22M0162 to Stanford University. S.K. was partly supported by NASA grants 80NSSC21K0735, 80NSSC19K0261, and 80NSSC20K0194 to NSO. Data-intensive computations in this work have utilized the High-Performance Computing facility at the Indian Institute of Astrophysics. A.S. is supported by INSPIRE Fellowship from the Department of Science and Technology (DST), Government of India. S.P.R. acknowledges support from the Science and Engineering Research Board (SERB, Government of India) grant CRG/2019/003786. We thank the anonymous referee for a thorough review and valuable suggestions that led to significant improvements and additions to the manuscript.

ORCID iDs

Anisha Sen https://orcid.org/0000-0003-2694-3288
S. P. Rajaguru https://orcid.org/0000-0003-0003-4561
Ruizhu Chen https://orcid.org/0000-0002-2632-130X
Junwei Zhao https://orcid.org/0000-0002-6308-872X
Shukur Kholikov https://orcid.org/0000-0003-1860-3697

References

Antia, H. M., & Basu, S. 2022, ApJ, 924, 19
Bisoi, S. K., & Janardhan, P. 2020, SoPh, 295, 79
Bobra, M. G., Sun, X., Hoeksema, J. T., et al. 2014, SoPh, 289, 3549
Braun, D. C. 2019, ApJ, 873, 94
Cameron, R. H., Dasi-Espuig, M., Jiang, J., et al. 2013, A&A, 557, A141
Cameron, R. H., & Schüssler, M. 2012, A&A, 548, A57
Chen, R., & Zhao, J. 2017, ApJ, 849, 144
Chen, R., & Zhao, J. 2018, ApJ, 853, 161
Couvidat, S., Schou, J., Hoeksema, J. T., et al. 2016, SoPh, 291, 1887
Dikpati, M., & Gilman, P. A. 2006, ApJ, 649, 498
Duvall, T. L., Jr. 1979, SoPh, 63, 3
Duvall, T. L., Jr., Jefferies, S. M., Harvey, J. W., & Pomerantz, M. A. 1993, Natur, 362, 430
Giles, P. M. 2000, PhD thesis, Stanford Univ., California
Giles, P. M., Duvall, T. L., Scherrer, P. H., & Bogart, R. S. 1997, Natur, 390, 52
Gottschling, N., Schunker, H., Birch, A. C., Löptien, B., & Gizon, L. 2021, A&A, 652, A148
Haber, D. A., Hindman, B. W., Toomre, J., & Thompson, M. J. 2004, SoPh, 220, 371
Hathaway, D. H., & Rightmire, L. 2010, Sci, 327, 1350
Hindman, B. W., Haber, D. A., & Toomre, J. 2009, ApJ, 698, 1749
Hoeksema, J. T., Baldner, C. S., Bush, R. I., Schou, J., & Scherrer, P. H. 2018, SoPh, 293, 45
Kholikov, S., Serebryanskiy, A., & Jackiewicz, J. 2014, ApJ, 784, 145
Komm, R. 2022, SoPh, 297, 99
Komm, R. W., Howard, R. F., & Harvey, J. W. 1993, SoPh, 147, 207
Liang, Z.-C., Birch, A. C., Duvall, T. L., Jr., Gizon, L., & Schou, J. 2017, A&A, 601, A46
Liang, Z.-C., & Chou, D.-Y. 2015, ApJ, 805, 165
Mackay, D. H., & Yeates, A. R. 2012, LRSP, 9, 6
Mahajan, S. S., Sun, X., & Zhao, J. 2023, ApJ, 950, 63
Norton, A. A., Charbonneau, P., & Passos, D. 2014, SSRv, 186, 251
Poulier, P. L., Liang, Z. C., Fournier, D., & Gizon, L. 2022, A&A, 664, A189
Rajaguru, S. P., & Antia, H. M. 2015, ApJ, 813, 114
Scherrer, P. H., Schou, J., Bush, R. I., et al. 2012, SoPh, 275, 207
Sen, A., & Rajaguru, S. P. 2023, ApJ, 956, 145
Sen, A., Rajaguru, S. P., Iyer, A. G., et al. 2025, ApJL, 984, L1
Toner, C., Goodrich, J., Shroff, C., & Kneale, R. 2004, in ESA Special Publication. 559, SOHO 14 Helio- and Asteroseismology: Towards a Golden Future, ed. D. Danesy, 657
Toner, C. G. 2001, in ESA Special Publication. 464, SOHO 10/GONG 2000 Workshop: Helio- and Asteroseismology at the Dawn of the Millennium, ed. A. Wilson & P. L. Pallé, 355
Wang, Y. M., Nash, A. G., & Sheeley, N. R., Jr. 1989, Sci, 245, 712
Yeates, A. R., Cheung, M. C. M., Jiang, J., Petrovay, K., & Wang, Y.-M. 2023, SSRv, 219, 31
Zhao, J., Bogart, R. S., Kosovichev, A. G., Duvall, T. L., Jr., & Hartlep, T. 2013, ApJL, 774, L29
Zhao, J., Couvidat, S., Bogart, R. S., et al. 2012b, SoPh, 275, 375
Zhao, J., Nagashima, K., Bogart, R. S., Kosovichev, A. G., & Duvall, T. L., Jr. 2012a, ApJL, 749, L5